1 **Instrument Artifacts Lead to Uncertainties in Parameterizations of Cloud**

2 **Condensation Nucleation**

3 **Jessica A. Mirrielees and Sarah D. Brooks**

4 Texas A&M University, College Station, TX 77843

5 Correspondence E-mail: jmirrielees@tamu.edu

6   **Abstract**

8   The concentrations of cloud condensation nuclei (CCN) modulate cloud properties, rainfall

9   location and intensity, and climate forcings. This work assesses uncertainties in CCN

10   measurements and the apparent hygroscopicity parameter (κ_{app}) which is widely used to represent

11   CCN populations in climate models. CCN measurements require accurate operation of three

12   instruments: the CCN instrument, the differential mobility analyzer (DMA), and the condensation

13   particle counter (CPC). Assessment of DMA operation showed that varying the ratio of aerosol to

14   sheath flow from 0.05 to 0.30 resulted in discrepancies between the κ_{app} values calculated from

15   CCN measurements and the literature value. Discrepancies were found to increase from effectively

16   zero to 0.18 for sodium chloride, and from effectively zero to 0.08 for ammonium sulfate. The

17   ratio of excess to sheath flow was also varied, which shifted the downstream aerosol distribution

18   towards smaller particle diameters (for excess flow < sheath flow) or larger particle diameters (for

19   excess flow > sheath flow) than predicted. For the CPC instrument, undercounting occurred at

20   high concentrations, resulting in calculated κ_{app} lower than the literature values. Lastly,

21   undercounting by CCN instruments at high concentration was also assessed, taking the effect of

22   supersaturation on counting efficiency into account. Under recommended operating conditions,

23   the combined DMA, CPC, and CCN uncertainties in κ_{app} are 1.1 % or less for 25 to 200 nm

24   diameter aerosols.

25 **Copyright Statement**

26 Will be provided by Copernicus

Introduction

29   Aerosol-cloud interactions represent a major uncertainty in current predictions of the Earth's climate

30   (IPCC, 2013). According to well-known Köhler theory, an aerosol's potential to catalyze cloud droplet

31   formation by activating as a cloud condensation nucleus (CCN) depends on its physical and chemical

32   properties. For any given composition, the CCN activation potential of an aerosol increases as its

33   diameter decreases. While the relationship between aerosol diameter and CCN activation is

34   straightforward, the effect of composition on an aerosol's ability to participate in cloud formation is

35   more complex (Petters and Kreidenweis, 2013; Ovadnevaite et al., 2011).   Predicting the cloud forming

36   capacity of various air masses based on the properties of the aerosol they contain is essential for

37   evaluating relative contributions from pollution, continental background and marine aerosol sources

38   (Brooks and Thornton, 2018; Carslaw et al., 2013). Long-term CCN measurements are available from

39   numerous locations globally (Schmale et al., 2018). However, understanding regional and temporal

40   variability in CCN populations requires the ability to assess whether observed differences reflect true

41   physical differences or simply variations in CCN sampling strategies.

43   Parameterizations of CCN activity which accurately prescribe CCN measurements are needed for

44   climate models, cloud resolving models, and air quality predictions (Betancourt and Nenes, 2014;

45   Betancourt et al., 2013; Chang et al., 2017; Crosbie et al., 2015; Karydis et al., 2012; Kawecki and

46   Steiner, 2018). One parameterization was designed to represent the cloud droplet activation potential

47   ambient aerosol masses of unknown composition with a single variable, kappa (κ) based on the dry

48   aerosol's hygroscopicity, or ability to uptake water and form a solution droplet (Petters and

49   Kreidenweis, 2007). Various names and abbreviations have been given to κ throughout the literature:

50   "hygroscopicity parameter", "single hygroscopicity parameter", κ (Petters and Kreidenweis, 2007;

51 Carrico et al., 2008;Asa-Awuku et al., 2010;Moore et al., 2012); "CCN-derived κ", κ_{CCN} (Carrico et al.,

52 2008; Petters and Kreidenweis, 2007); and the "apparent hygroscopicity parameter" κ_{app} (Sullivan et

53 al., 2009; Collins et al., 2016; Petters and Kreidenweis, 2013). The term *apparent* hygroscopicity is

54 favored by many because it emphasizes that fact that while CCN activation can often be predicted

55 accurately by hygroscopic water uptake, they are different physical processes. It is possible for a

56 compound to have high intrinsic hygroscopicity and low apparent hygroscopicity if it is poorly soluble

57 in water (Sullivan et al., 2009).

58

59 Once calculated, hygroscopicity parameters are useful tools for comparing CCN field measurements

60 conducted in various regions and seasons and for making predictions about cloud formation, aerosol-

61 cloud interactions in weather, and climate models. Values of κ_{app} can be used to compare the CCN

62 results in field and laboratory studies, including sea spray aerosol. For example, aggregation of results

63 from several mesocosm experiments and marine field studies found submicron (30-100 nm) κ_{app} for sea

64 spray aerosol as low as 0.4 and as high 1.3 (Collins et al., 2016).

65

66 Several studies have examined the sensitivity of models to κ values derived from HTDMA

67 measurements. An analysis of the NASA Global Modeling Initiative Chemical Transport Model and the

68 GEOS-Chem CTM (Karydis et al., 2012) found that cloud droplet number concentration is sensitive to κ

69 in Arctic and remote regions, where background aerosol loadings are low. Another study (Betancourt

70 and Nenes, 2014) found that a ±50 % uncertainty range in the κ of secondary organic aerosols and

71 particulate organic matter resulted in a cloud droplet number concentration uncertainty of up to 15 %

72 and 16 %, respectively. Updating precipitation models with lab-derived κ values for specific inorganic

73 and organic species may increase the accuracy of storm forecasts by providing better predictions of

74 intense precipitation (Kawecki and Steiner, 2018). In terms of climate, (Liu and Wang, 2010) found that

75   increasing the κ of primary organic aerosols from 0 to 0.1, and decreasing the κ of secondary organics

76   aerosols from 0.14 to 0.07, resulted in an uncertainty in global secondary aerosol indirect forcing of 0.4

77   Wm^{-2} from pre-industrial times to present day.

78

79   The sensitivity of weather and climate models to hygroscopicity parameters demonstrates the need for

80   accurate measurements. In this study, we examine experimental uncertainties in CCN measurements and

81   the resulting uncertainties in determination of κ_{app}. Differences in report κ_{app} values may result from

82   experimental artifacts rather any actual differences in aerosol's ability to facilitate cloud formation. By

83   systematically quantifying sources of experimental error, this study provides a framework for

84   determining the significance of variations in CCN properties reported in multiple studies and defining

85   the operating conditions which minimize instrumental artifacts.

86

87   **1. Background**

88

89   The Köhler equation relates water vapor saturation at the surface of a wet droplet, s, to its radius at

90   equilibrium (Rogers and Yau, 1989):

91

92    $$s = \left(1 - \frac{b}{r^3}\right) \exp\left(\frac{a}{r}\right) \qquad (1a)$$

93

94    $$a = \frac{2\sigma_w M_w}{\rho_w RT} \qquad (1b)$$

95

96    $$b = \frac{3 i m_s M_w}{4\pi \rho_w M_s} \qquad (1c)$$

97

98   where s is the equilibrium saturation ratio of a solution droplet with radius r, σ_w is the surface tension of

99   water, M_w is the molecular weight of water, R is the ideal gas constant, T is temperature in Kelvin, ρ_w is

100   the density of water, and M_s is the molecular weight of the solute. The minimum saturation ratio that is

101   required for spontaneous droplet growth, s_{act}, is therefore:

102

103   $$s_{crit} = 1 + \sqrt{\frac{4a^3}{27b}} \qquad (2)$$

104

105   Petters and Kreidenweis [2007] reformulated the Köhler equation as κ-Köhler theory:

106

107   $$s_{crit} = exp\left(\sqrt{\frac{4A^3}{27 D_{act}^3 \kappa_{app}}}\right) \qquad (3a)$$

108   and

109

$$A = \frac{4\sigma_{lv}M_w}{RT\rho_w} \tag{3b}$$

111

112 Where s_{crit} is the critical water vapor saturation, D_{act} is the dry particle activation diameter and κ_{app} is

113 the apparent hygroscopicity parameter. Solving for κ_{app} yields:

114

$$\kappa_{app} = \frac{4A^3\sigma_{lv}^3}{27T^3D_{act}^3\ln^2(s_{crit})} \tag{4}$$

116

117 The apparent hygroscopicity parameter can be calculated from experimental CCN results, where the dry

118 diameter and water vapor saturation are known. For a chosen aerosol diameter, the activated fraction is

119 the ratio of the concentration aerosols that activate as CCN to the total aerosol concentration:

120

$$Activated\ fraction = \frac{CCN\ Concentration}{Aerosol\ Concentration} \tag{5}$$

122

123 Activated fraction data is fit with a sigmoid error function to determine the supersaturation at which 50

124 % of the particles have activated as CCN, which is considered the operationally defined critical

125 supersaturation SS_{crit} (Rose et al., 2008). The critical saturation s_{crit} can then be determined and

126 entered into Eq. (4) in order to calculate κ_{app} for the near-monodisperse aerosol:

127

$$s_{crit} = 1 + \frac{SS_{crit}}{100} \tag{6}$$

129

130   Reporting κ_{app} as a function of diameter allows for the comparison of the cloud condensation nucleation

131   abilities of multimodal aerosol populations, without overlooking differences which arise due to aerosol

132   composition.

133

134   The apparent hygroscopicity parameter is related to chemical composition; therefore, the calculated κ_{app}

135   of a pure substance should be constant across CCN experiments. However, discrepancies between κ_{app}

136   for a single chemical species have been observed. Experimental results for ammonium nitrate are

137   inconsistent $0.577 \leq \kappa_{app} \leq 0.753$, and large ranges are often observed for organic compounds, such

138   as glutaric acid ($0.054 \leq \kappa_{app} \leq 0.16$) and malonic acid ($0.199 \leq \kappa_{app} \leq 0.255$) (Koehler et al.,

139   2006;Kumar et al., 2003;Hartz et al., 2006;Svenningsson et al., 2006). Below we evaluate potential

140   sources of uncertainties in CCN measurements and the resulting uncertainties in κ_{app}.

141

142   **2. Artifacts derived from CCN measurements**

143

144   CCN measurements require accurate operation of three instruments: the CCN, the differential mobility

145   analyzer (DMA), and the condensational particle counter (CPC). The setup for laboratory CCN

146   experiments is shown in Fig. 1. First, a polydisperse population of aerosols is generated by an atomizer

147   and dried using a desiccant tube packed with silica gel. A near-monodisperse flow is obtained through

148   size-selection in the DMA. The flow is then split between a CPC (which measures aerosol

149   concentration) and a CCN counter (which measures the concentration of particles that activate as cloud

150   condensation nuclei at a given percent water vapor supersaturation).

151

152

153

154   **2.1 Artifacts derived from differential mobility analyzers**

155

156   **2.1.1   DMA operation and electrical mobility**

157

158   Differential mobility analyzers used in atmospheric science include commercially available instruments

159   from Grimm Aerosol Technik, TSI Incorporated, and MSP Corporation. They have also been custom

160   built by a number of research groups (Mei et al., 2011;Barmpounis et al., 2016;Jokinen and Makela,

161   1997;Seol et al., 2000). All models allow for the selection of particles through electrical mobility, the

162   ability of a particle to move through a medium (such as air) while acted upon by an electrical field. The

163   DMA size-selects near-monodisperse aerosol from a polydisperse aerosol source, as shown in Fig. 2

164   (modeled after the Vienna-type long Differential Mobility Analyzer from Grimm Technologies). The

165   electrical mobility Z_p of a particle with mobility diameter d_m can be calculated according to:

166

$$Z_p = \frac{neC_C(d_m)}{3\pi\eta d_m} \qquad (7)$$

168

169 where n is the number of charges on the particle (assumed to be one in this study), e is the elementary

170 unit of charge, η is the gas dynamic viscosity, and $C_C(d_m)$ is the Cunningham slip correction factor:

171

$$C_C(d_m) = 1 + \frac{2\lambda}{d_m}\left(\alpha_{CC} + \beta_{CC}\exp\left[-\frac{\gamma_{CC}}{2\lambda/d_m}\right]\right) \qquad (8)$$

173

174 where λ is the mean free path (DeCarlo et al., 2004). For the Vienna-type long Differential Mobility

175 Analyzer from Grimm Technologies, Inc. considered here, $\alpha_{CC} = 1.246$, $\beta_{CC} = 0.42$, and $\gamma_{CC} = 0.86$

176 (Grimm Aerosol Technik, 2009).

177

178 Particle-laden flow enters the differential mobility analyzer through the aerosol inlet (flow Q_a), and travels

179 down the DMA column (inner radius r_1, outer radius r_2) with the clean air sheath flow Q_{sh}. Positively-

180 charged particles are attracted by the negatively-charged inner electrode, to which voltage V_0 has been

181 applied. Ideally, selection of a voltage allows only particles of a specific mobility diameter to exit the

182 DMA through the sample flow Q_s. All particles with larger diameter (lower Z_p) or smaller diameter

183 (higher Z_p) will exit the DMA through the excess flow Q_e. In other words, Q_s would ideally be a truly

184 monodisperse flow.

185

186 In reality, the aerosol flow that leaves the DMA through Q_s is polydisperse with a mobility distribution

187 determined by instrumental parameters. A triangular approximation has been chosen as a model for this

188 distribution, as particle inertia is negligible for the diameters considered in this study (Stratmann et al.,

189   1997;Mamakos et al., 2007). The probability that a particle at the aerosol inlet will exit with the sampling

190   flow is defined by transfer function $f\left(Z_p, Z_{p,mid}\right)$:

191

192     $$f\left(Z_p, Z_{p,mid}\right) = \frac{\alpha_{TF}}{2\beta_{TF}}\left(\left|\frac{Z_p}{Z_{p,mid}} - (1 + \beta_{TF})\right| + \left|\frac{Z_p}{Z_{p,mid}} - (1 - \beta_{TF})\right| - 2\left|\frac{Z_p}{Z_{p,mid}} - 1\right|\right) \qquad (9)$$

193   where $Z_{p,mid}$ is the midpoint mobility of the transfer function, and α_{TF} and β_{TF} are flow-derived

194   constants, defined as:

195

196     $$\alpha_{TF} = \frac{Q_s + Q_a}{2Q_a} \qquad (10a)$$

197   and

198     $$\beta_{TF} = \frac{Q_s}{Q_{sh}} \qquad (10b)$$

199

200   The midpoint and half-width of the transfer function are respectively calculated according to: (Knutson

201   and Whitby, 1975)

202     $$Z_{p,mid} = \frac{Q_e + Q_{sh}}{4\pi L V_0}\ln\left(\frac{r_2}{r_1}\right) \qquad (11a)$$

203   and

204

205     $$\Delta Z_p = \frac{Q_a}{2\pi L V_0}\ln\left(\frac{r_2}{r_1}\right) \qquad (11b)$$

206

207

208

2.1.2 κ_{app} artifact analysis and results

209

210

211 Next we assess the ramifications of the DMA transfer function for the derived κ_{app}. A lognormal

212 theoretical aerosol number distribution was used to represent a polydisperse ambient aerosol population

213 (Fig. 3a). This distribution was converted to an electrical mobility distribution using Eq. (7) and Eq. (8),

214 assuming that the aerosols in the distribution were spherical and singly charged. From the distribution, a

215 series of single aerosol sizes were selected (25, 50, 100, and 200 nm diameter). For each aerosol size,

216 the resulting DMA transfer functions were calculated for 7 cases using Eq. (9) and the various

217 parameters for DMA sheath, excess, aerosol, and sample flow listed in Table 1. For example, the

218 resulting DMA transfer functions for a 100 nm aerosol conditions constrained by Cases 1-4 are shown in

219 Fig. 3b, where an increase in Q_a/Q_{sh} from 0.1 (black line) to 0.3 (green line) tripled the width of the

220 number distribution, and decreasing Q_a/Q_{sh} to 0.05 (blue line) from 0.10 halved the width of the

221 number distribution. The result of applying the transfer functions shown in Fig. 3b to the distribution in

222 Fig. 3a is shown in Fig. 3c.

223

224 All downstream distributions for all seven DMA cases and all aerosol sizes are shown in Fig. S1 in the

225 Supplement. DMA Cases 1-4 represent experimental conditions in which the sheath and excess air

226 flows are equal and the aerosol/sheath flow ratio is varied. As Q_a/Q_{sh} increases, the width of the

227 number distribution measured downstream of the DMA increases, while the midpoint diameter remains

228 constant. It was found that doubling the aerosol to sheath ratio doubled the width of the downstream

229 number distribution for 25, 50, 100, and 200 nm particles. For example, when selecting 200 nm

230 particles, increasing Q_a/Q_{sh} from 0.10 to 0.20 increased the downstream diameter range from 181-222

231 nm (a spread of 41 nm) to 167-250 nm (a spread of 87 nm). The particle diameter ranges that would be

232 observed downstream of the DMA are summarized in Table 2.

233

234   To assess the variations in CCN properties resulting from DMA uncertainties the critical supersaturation

235   were calculated for representative atmospheric aerosols. The value of SS_{crit} was calculated for each

236   particle diameter using Eq. (3a), using literature values for apparent hygroscopicity of 0.61 for

237   ammonium sulfate and 1.28 for sodium chloride (Clegg et al., 1998). It should be noted that this

238   analysis considers two homogeneous aerosol distributions of hygroscopic salts. Real aerosol

239   distributions tend to be mixtures of many species, and the shape of the number distribution can vary

240   between species.

241

242   Note that in the absence of DMA diameter uncertainty, this single component aerosol population should

243   be characterized by a single κ_{app} regardless of diameter. To test how uncertainties in DMA diameter

244   translate to uncertainties in κ_{app}, the true critical saturation ratio s_{crit} was then put into Eq. (4) in order

245   to calculate the "perceived" κ_{app} for each diameter given the chosen transfer function from Cases 1-7.

246   For example, if 100 nm particles were selected from the DMA by the user, the transfer functions would

247   allow larger and smaller particles to pass into the sample flow, as shown in Table 2. Particles with

248   diameter > 100 nm would be "perceived" to have higher apparent hygroscopicity than particles with

249   diameter < 100 nm, since the equilibrium vapor pressure over the surface of a particle decreases as its

250   diameter increases (and as curvature decreases). Using Eq. (12), these diameter-specific "perceived"

251   κ_{app} values were volume-weighted, resulting in $\kappa_{app,theory}$:

252

253
$$\kappa_{app,theory} = \sum_i \epsilon_i \kappa_i \tag{12}$$

254

255   Results for ammonium sulfate and sodium chloride are shown in Fig. 4a. The critical saturation ratio

256   was calculated from $\kappa_{app,theory}$ using Eq. (3a) for each case and converted to critical supersaturation.

257   The results are compared to theoretical κ-Köhler theory curves for ammonium sulfate and sodium

258   chloride generated using the literature κ_{app} for each compound (Fig. 4b).

259

260   Discrepancies between $\kappa_{app,theory}$ calculated in this study and literature values (hereon referred to as

261   "κ_{app} artifacts") are shown for both compounds in Fig. 4c-d.

262

263   The greatest κ_{app} artifacts were found in DMA case 4 (where the aerosol/sheath ratio was the highest)

264   for both ammonium sulfate and sodium chloride aerosols. The artifacts for ammonium sulfate in DMA

265   case 4 were 0.05-0.08, or 8-13 % of the literature value used for $\kappa_{app}^{(NH_4)_2SO_4}$, while the sodium chloride

266   artifacts in DMA case 4 were 0.11-0.18, or 9-14 % of the literature value used for κ_{app}^{NaCl}. Artifacts were

267   also high for DMA case 6 ($-0.025 \leq \kappa_{app,artifact}^{(NH_4)_2SO_4} \leq -0.018$) and DMA case 7 ($0.016 \leq$

268    $\kappa_{app,artifact}^{(NH_4)_2SO_4} \leq 0.017$), where $Q_e > Q_{sh}$.

269

270   κ_{app} artifacts were larger for sodium chloride ($-0.05 \leq \kappa_{app,artifact}^{NaCl} \leq 0.18, 4-14$ % of κ_{app}^{NaCl}) than

271   for ammonium sulfate ($-0.03 \leq \kappa_{app,artifact}^{(NH_4)_2SO_4} \leq 0.08, 5-13$ % of $\kappa_{app}^{(NH_4)_2SO_4}$) across the DMA cases.

272   As our results show, when two or more compounds are compared, the more hygroscopic compound will

273   have larger κ_{app} artifacts.

274 **3. Artifacts derived from condensation particle counters**

275

276 **3.1. CPC operation at low concentration**

277

278 The second instrument which must function accurately during CCN experiments is the condensation

279 particle counter. CPC performance is characterized by the maximum counting efficiency (which may be

280 influenced by the working fluid in the instrument) and the 50 %-cut-off diameter (d_{50}), the particle

281 diameter at which 50 % counting efficiency is observed, both of which can vary between commercially

282 available models and even between individual CPCs (Heim et al., 2004). One study found that n-

283 butanol CPCs (TSI, Inc. Models 3772, 3775, and 3776) exhibited smaller d_{50} for silver particles than

284 sodium chloride ($3.3\ nm \leq d_{50}^{Ag} \leq 7.8\ nm$ and $4.1\ nm \leq d_{50}^{NaCl} \leq 14.7\ nm$), due to the more effective

285 condensation of n-butanol on silver particles (Hermann et al., 2007).

286

287 Maximum counting efficiencies in that study varied from 88.9 % to 100.3 %. Another comparison of n-

288 butanol CPCs (TSI Inc. Models 3010 and 3022, Grimm Tech. Inc. Model 5.403) found $3.1\ nm \leq d_{50} \leq$

289 $11.9\ nm$ for sodium chloride aerosols (Heim et al., 2004). In another study, the counting efficiencies

290 observed in measurements of tungsten oxide particles by different instruments of the same model (TSI

291 3025) varied from 88.9 % to 138.9 %, while $d_{50}^{WO_x}$ varied from 3.2 nm to 11.0 nm (Hameri et al., 2002).

292

293 While some issues can cause undercounting at all concentrations, the additional issue of uncounted

294 particles due to the arrival of more than one particle in the detector's field of view at any time arises

295 only at higher concentrations. The cut-off between "low" and "high" concentration is not exact and

296 varies between instruments. CPC undercounting issues which arise even at relatively low concentrations

297 will be discussed in this section, and concentration-dependent effects will be explored in Sect. 3.2.

298

299   Six counting efficiency curves were generated using sigmoidal distributions and the 50 % cut-off

300   diameters and maximum counting efficiencies listed in Table 3. Chosen values represent d_{50} values and

301   maximum counting efficiencies reported in the literature under relatively low concentrations of 1000-

302   4000 cm^{-3} (Hermann et al., 2007). The resulting sigmoidal distributions (Fig. 5a) were used to

303   determine the counting efficiency of 25, 50, 100, and 200 nm particles.

304

305   Next, κ_{app} was calculated from theoretical critical supersaturations for each chosen diameter. To do so,

306   four sigmoid curves representing sodium chloride CCN activation (hereon referred to as "activation

307   curves") for 25, 50, 100, and 200 nm were generated. The κ-Köhler-derived critical supersaturation of

308   sodium chloride was used as the midpoint of each activation curve, and one-tenth of this value was used

309   as the standard deviation (100 % CE, Fig. 5b-e). These values are consistent with the standard

310   deviation/midpoint ratio observed from our instrument's ammonium sulfate CCN calibration data.

311

312   Activation curves were then generated for CPC Cases 1-6 by dividing the activated fraction for each dry

313   particle diameter by the counting efficiency for that diameter. Critical supersaturation was determined

314   for each CPC case. Results are summarized in Fig. 5f. Next, critical supersaturation was converted to

315   saturation, and $\kappa_{app,theory}$ was calculated for each diameter in each CPC Case using Eq. (4) (see Fig.

316   5g). As above, κ_{app} artifacts were calculated by finding the difference between these results and the

317   literature value of κ_{app} for sodium chloride (see Fig. 5h).

318

319   For the diameters studied, the effect of maximum counting efficiency on CPC concentration (and

320   activated fraction) is greater than the effect of 50 %-cutoff diameter. However, neither characteristic

321   resulted in large κ_{app} artifacts. The largest κ_{app} artifact observed at "low" concentrations was 0.035 for

322   CPC Case 4, 2.4 % of the literature value for the apparent hygroscopicity factor for sodium chloride.

323 **3.2. CPC operation at high concentration**

324

325 Operation at high concentrations introduces an additional source of undercounting through particle

326 coincidence at the CPC optical counter. For the TSI 3010 CPC, undercounting is observed is for particle

327 concentrations above $1 \times 10^4 \, cm^{-3}$. At $5 \times 10^4 \, cm^{-3}$, the detector saturates and cannot detect higher

328 concentrations. By comparison, the TSI 3025 is effective at counting higher particle concentrations, of

329 up to $2.5 \times 10^4 \, cm^{-3}$ (Hameri et al., 2002;Sem, 2002).

330

331 To model undercounting due to particle coincidence, four CPC counting curves (Fig. 6a) were generated

332 using the equations in Table 4. Case 7 represents a CPC where counting efficiency decreases with

333 particle concentration, without reaching saturation. Cases 8-10 represent CPCs were saturation is

334 reached at $4 \times 10^4 \, cm^{-3}$, $2 \times 10^4 \, cm^{-3}$, and $1 \times 10^4 \, cm^{-3}$, respectively. These saturation

335 concentrations are of similar magnitude to those observed from TSI 3010 concentration data.

336

337 In all cases, the aerosol population was assumed to be a distribution consisting of 5×10^6 particles/cm^3

338 with a peak concentration at 50 nm (Fig. 6b). Each case was applied to this theoretical distribution in

339 order to determine the concentration measured by the CPC for 25, 50, 100 and 200 nm aerosols. Then,

340 the counting efficiency was calculated for each case and aerosol diameter.

341

342 Sigmoidal activated fraction curves were generated for 25, 50, 100 and 200 nm sodium chloride

343 aerosols. As in the low concentration cases, the midpoint of each 100 % CE curve was chosen to be

344 equal to the κ-Köhler-derived critical supersaturation of sodium chloride at each dry diameter, and the

345 standard deviation of each curve is equal to one-tenth of the critical supersaturation. These activated

346 fraction curves were adjusted using the counting efficiencies calculated in the previous step. In cases

347   where the activated fraction has increased due to undercounting by the CPC, the theoretical sigmoidal

348   curve shifts to the left relative to the 100 % CE case (Fig. 7c-f). Thus, undercounting by the CPC

349   effectively increases the reported activated fraction. As above, critical supersaturation was determined

350   from each of these curves, and $\kappa_{app,theory}$ was subsequently calculated using Eq. (4) (Fig. 7g-h).

351

352    $\kappa_{app,theory}$ fell over a much wider range for 25, 50, and 100 nm particles (1.30-1.56, 1.32-1.70, and

353   1.30-1.55, respectively) than for 200 nm particles (1.28-1.29) due to the lower concentration of 200 nm

354   particles in the chosen aerosol distribution, which resulted in a higher counting efficiency for these

355   aerosols. In comparison, the largest range in $\kappa_{app,theory}$ was observed for 50 nm aerosols, the peak

356   diameter in this aerosol distribution.

357

358   A wider range in $\kappa_{app,theory}$ was observed for the high-concentration CPC Cases (7-10) compared to the

359   low-concentration CPC Cases (1-6). The lowest counting efficiency observed across the low-

360   concentration cases was 89.9 % for 25 nm aerosol in Case 4, while the lowest counting efficiency

361   observed in the high-concentration cases was 18.0 % for 50 nm aerosol in Case 10.

362

363   Artifacts in the apparent hygroscopicity parameter are shown in Fig. 6i. κ_{app} artifacts were the greatest

364   for a CPC that becomes saturated at 20,000 particles/cm^3 (0.0131 $\leq \kappa_{app} \leq$ 0.4206). The lower the

365   concentration at which a CPC becomes saturated, the more quickly its counting efficiency will drop as

366   concentration increases, resulting in increased activated fraction and increased apparent hygroscopicity.

367   The magnitude of artifacts due to CPC undercounting depends on the saturation concentration of the

368   CPC and the distribution of the aerosol population being studied.

369

370

4. Artifacts derived from cloud condensation nuclei instruments

Finally, the third instrument whose performance accuracy contributes to the overall certainty in CCN

assessment in the CCN instrument itself. Several instruments have been implemented for measuring

CCN concentrations over the last few decades. Older models include the Continuous Flow Parallel Plate

Diffusion Chamber (Sinnarwalla, 1973) and the Hudson CCN spectrometer (Hudson, 1989) which both

employ an applied temperature gradient perpendicular to the aerosol flow. Newer models, such as the

widely-used Droplet Measurement Technology Cloud Condensation Nuclei Counter (DMT CCN-100),

operate with a streamwise temperature gradient and continuous, laminar flow (Lance et al., 2006). The

following analysis considers the DMT CCN-100. According to the CCN-100 manual, the counting

efficiency for this CCN instrument depends on concentration and supersaturation (Fig. 6a). The

counting efficiency decreases rapidly with concentration at < 0.2 % SS due to rapid water vapor

depletion at these low supersaturations, and falls off more slowly for > 0.2 % SS (DMT CCN-100

manual).

The counting efficiency of the DMT CCN-100 was tested for four lognormal aerosol distributions with

peak concentrations at 50 nm and varying total concentrations (Table 5, Fig. 7b). Note that for

comparison, CCN Case 1 was chosen to be identical to the aerosol distribution used for the high-

concentration CPC cases. CCN Cases 2-4 follow the same distribution shape, with decreased total

particle concentration.

The counting efficiencies for each case were applied to theoretical sodium chloride sigmoidal activated

fraction curves to produce normalized activated fraction curves (Fig. 8c-f). As above, the midpoint is

set to the critical supersaturation of sodium chloride at each dry diameter, and the standard deviation is

395   assumed to be one-tenth of the critical supersaturation. CCN undercounting effectively decreases

396   activated fraction, therefore shifting the activated fraction curve downwards and towards higher percent

397   supersaturations. The opposite effect is observed when CPC undercounting occurs. Critical

398   supersaturation was determined for each CCN case, as above (Fig. 7g). Values of SS_{crit} were then

399   converted to saturation, and $\kappa_{app,theory}$ was calculated using Eq. (4) (Fig. 7h).

400

401   Significant deviations from κ-Köhler theory were only observed in CCN Case 1, with total aerosol

402   concentration 5×10^6 particles/cm^3 (Fig. 8g-i). The largest deviation for CCN Case 1 was observed in

403   100 nm particles ($\kappa_{app,artifact} = -0.57$), due to the higher concentration of 100 nm particles compared

404   to 25 and 200 nm particles, and the lower supersaturation necessary for activation. The largest artifacts

405   across CCN Cases 2 and 3 were also observed for 100 nm particles, though no artifacts were observed

406   for any particle diameter in CCN Case 4 due to the much lower concentrations.

407

408   Sodium chloride is very hygroscopic. It should be noted that aerosols consisting of less hygroscopic

409   compounds will activate at higher supersaturations (> 0.2 % SS regime) which will lead to smaller κ_{app}

410   artifacts when the same aerosol distribution and total aerosol concentration is considered. If a mixture

411   was considered (for example, sodium chloride with a non-hygroscopic species such as soot) the results

412   may also be different. The shape of the aerosol distribution must also be taken into account. A

413   distribution with a narrower peak than the one generated for this analysis would be at risk for larger

414   κ_{app} artifacts for any total aerosol concentration, and these artifacts would be greater at the peak

415   diameter, while a broader distribution would result in less variation in κ_{app} artifacts for each particle

416   diameter.

417   **5.   Discussion**

418

419   A comparison of several instrument sources of error in CCN-derived κ_{app} is shown in Fig. 8. DMA

420   Case 4, CPC Case 4, CPC Case 10, and CCN Case 1 represent the operating conditions that resulted in

421   the largest κ_{app} artifacts in this study. In DMA Case 4, the aerosol/sheath ratio of 0.30 resulted in a

422   broadened aerosol distribution downstream of the DMA. Compared to DMA Case 1, where

423   $Q_a/Q_{sh} = 0.10$, the downstream diameter range in DMA Case 4 was 300 % higher for 25 nm particles,

424   resulting in a spread of 20-36 nm.   Similarly, the diameter ranges for 50, 100, and 200 nm diameter

425   were 220 %, 230 %, and 220 % wider than in Case 1, respectively. Compared to the most ideal DMA

426   case presented in this study (DMA Case 2), where $Q_a/Q_{sh} = 0.05$, the downstream diameter range in

427   DMA Case 4 was 700 % higher for 25 nm particles; the diameter ranges for 50, 100, and 200 nm

428   diameter were 540 %, 560 %, and 520 % wider than in Case 2, respectively.

429

430   CPC Case 4 represents κ_{app} artifacts (0.031-0.035) due to undercounting that arises from poor

431   maximum CPC counting efficiency (90 %), which may be observed when using butanol as a working

432   fluid while measuring the concentration of inorganic aerosols. In contrast, κ_{app} artifacts are negligible

433   (< 0.10 % of κ_{app}^{NaCl}) in CPC Case 3, where maximum counting efficiency = 100 %. CPC Cases 8 and 10

434   represent undercounting at high concentration with CPCs where saturation is observed at $4 \times 10^4 cm^{-3}$

435   and $1 \times 10^4 cm^{-3}$, respectively. Counting efficiency drops off more rapidly with concentration in the

436   latter case, resulting in κ_{app} artifacts that are highest at the peak of the aerosol distribution (0.1190 and

437   0.4206 for 50 nm aerosols in CPC Cases 8 and 10, respectively).

438

439   CCN Case 1 represents CCN undercounting at high concentration (total aerosol concentration = $5 \times$

440   $10^6 cm^{-3}$). CCN undercounting is greatest for low supersaturation (< 0.2 %) and high concentration,

441   resulting in the lowest counting efficiency and highest κ_{app} artifacts (- 0.57) for 100 nm aerosols in

442   CCN Case 1. The largest CCN-derived κ_{app} artifact observed outside of CCN Case 1 was -0.01 for

443   100 nm aerosols in CCN Case 2.

444

445   The combined artifacts for the cases where the highest artifacts were observed (DMA Case 4, CPC Case

446   4, CPC Case 10, CCN Case 1) are 0.21, 0.24, 0.32, and 0.21 for 25, 50, 100, and 200 nm particles

447   respectively, as shown in Fig. 8. The combined artifacts for the lowest-artifact cases (DMA Case 2,

448   CPC Case 3, and CCN Case 4) are < 0.001 except for 200 nm particles, where $\kappa_{app,artifact} = 0.0013$.

449   **Conclusions**

450

451   The sensitivity of weather and climate models to accuracy in CCN activation predictions has been

452   demonstrated in other works. Possible sources of apparent hygroscopicity artifacts calculated from CCN

453   measurements have been presented in this study. This analysis has focused on sodium chloride and

454   ammonium sulfate aerosols, but it can be extended to other aerosol populations, including mixtures and

455   field samples.

456

457   The largest artifacts ($-0.57 < \kappa_{app,artifact} < 0.42$) in this study arise from undercounting by

458   condensation particle counters and cloud condensation nuclei counters at high concentration. This

459   problem arises in cases which represent attempts to measure aerosol concentrations much higher than

460   are recommended for these instruments, ~10^4 cm^{-3} (CPC Cases 7-10 and CCN Case 4). Corrective

461   action should be taken to dilute aerosol samples in order to avoid undercounting.

462

463   Smaller artifacts ($\kappa_{app,artifact} < 0.04$) were observed for the CPC cases where 50 %-cut-off diameter

464   and maximum counting efficiency were varied. Given the chosen particle diameters (25, 50, 100, 200

465   nm), κ_{app} artifacts due to d_{50} were minimal. The largest κ_{app} artifacts for a CPC counting at low

466   concentration (0.031-0.035) were observed where the maximum counting efficiency was equal 0.90.

467   This may represent a compositional mismatch between n-butanol as the working fluid and sodium

468   chloride as the aerosol, due to the poor solubility of the latter in the former. Individual n-butanol CPCs

469   may exhibit higher maximum counting efficiencies for sodium chloride.

470

471   Uncertainty arising from the DMA depended greatly on the chosen aerosol and sheath settings. One set

472   of DMA cases (Cases 2-4) examined the effect of aerosol/sheath ratio. By decreasing this ratio, a

473   narrower near-monodisperse flow can be produced, which increases the accuracy of calculated κ_{app}.

474   The κ_{app} artifacts for an aerosol/sheath ratio of 0.10 were 1.1 % of $\kappa_{literature}$ for 25 nm sodium

475   chloride aerosols, 0.93 % for 50 nm, 0.81 % for 100 nm, and 0.66 % for 200 nm. Decreasing the

476   aerosol/sheath ratio to 0.05 resulted in $\kappa_{app} \approx 0.01$ % of $\kappa_{literature}$ for NaCl. When a ratio of 0.30 was

477   employed, the resulting artifacts that were ~10 % of $\kappa_{literature}$ for sodium chloride.

478

479   The second set of DMA cases (5-7) were designed to evaluate the effects of holding the sheath flow

480   constant while varying the excess air flow by -2 %, +2 %, and +5 %. These resulted in shifts of ≤ 2 nm

481   for 25 nm and 50 nm particles, ≤ 4 nm for 100 nm particles, and ≤ 7 nm for 200 nm particles. The

482   downstream aerosol distribution was shifted towards larger particle diameters when sheath flow

483   exceeded excess flow, and towards smaller particle diameter when sheath flow was less than excess

484   flow. When taking field measurements, the composition of the sample may vary with particle diameter,

485   thereby introducing another source of error from a broader DMA distribution.

486

487   Under optimal operating conditions, where the DMA sample/sheath ratio is 0.10 and excess/sheath ratio

488   is 1.0, and in the absence of undercounting by the CPC or CCN, uncertainties in κ_{app} are within ±1.1 %

489   for 25 to 200 nm aerosols. When the DMA sample/sheath ratio drops to 0.05, κ_{app} uncertainties

490   decrease to ±0.01 %.

491

492   Apparent hygroscopicity parameter artifacts were calculated for two pure, inorganic species in this

493   study. This analysis could be used to estimate κ_{app} artifacts for ambient aerosol populations, which

494   may result in a better understanding of the "real" differences between these populations. As discussed in

495   the introduction, Collins et al. 2016 aggregated κ_{app} from several mesocosm and field studies for 30-

496   100 nm sea spray aerosol ($0.4 < \kappa_{app}^{SSA} < 1.3$). The wide range of κ_{app} in these studies may be

497   attributed to differences in composition, experimental artifacts, or a combination of the two.

498   Quantification of experimental artifacts would facilitate interpretation of κ_{app} in aerosol populations and

499   constrain the importance of composition in CCN activation. There has been a recent proliferation of

500   CCN data availability from multiple researchers and multiple experimental setups. To maximize the

501   utility of these studies and to compare cloud-activating properties of various ambient aerosol masses, it

502   is essential that artifacts are considered in both CCN data collection and in reporting of the data.

503 Supplement Link

504 Will be included by Copernicus

505

506 Author Contribution

507 Sarah D. Brooks provided the conceptual framework and reviewed the manuscript. Jessica A. Mirrielees

508 performed the analysis and wrote the manuscript.

509

510 Competing Interests

511 The authors declare that they have no conflict of interest.

512

513 Disclaimer

514 Will be included by Copernicus

515

516 Acknowledgements

517 This project was supported by the National Science Foundation of the United States (Award

518 #15398810). In addition, Mirrielees thanks Texas A&M University for support through Institute for and

519 Advanced Studies HEEP PhD Fellowship and a Lechner Scholarship.

References

Asa-Awuku, A., Nenes, A., Gao, S., Flagan, R. C., and Seinfeld, J. H.: Water-soluble SOA from Alkene ozonolysis: composition and droplet activation kinetics inferences from analysis of CCN activity, Atmos. Chem. Phys., 10, 1585-1597, 10.5194/acp-10-1585-2010, 2010.

Barmpounis, K., Maisser, A., Schmidt-Ott, A., and Biskos, G.: Lightweight differential mobility analyzers: Toward new and inexpensive manufacturing methods, Aerosol Sci. Technol., 50, 4, 10.1080/02786826.2015.1130216, 2016.

Betancourt, R. M., Nenes, A., and Liu, X. H.: Relative Contributions of Aerosol Properties to Cloud Droplet Number: Adjoint Sensitivity Approach in a GCM, in: AIP Conference Proceedings, 19th International Conference on Nucleation and Atmospheric Aerosols (ICNAA), Colorado State Univ, Ctr Arts, Fort Collins, CO, 2013, WOS:000319766400170, 679-682, 2013.

Betancourt, R. M., and Nenes, A.: Understanding the contributions of aerosol properties and parameterization discrepancies to droplet number variability in a global climate model, Atmos. Chem. Phys., 14, 4809-4826, 10.5194/acp-14-4809-2014, 2014.

Brooks, S. D., and Thornton, D. C. O.: Marine Aerosols and Clouds, in: Annual Review of Marine Sciences, Vol 10, edited by: Carlson, C. A., and Giovannoni, S. J., Annual Review of Marine Science, 289-313, 2018.

Carrico, C. M., Petters, M. D., Kreidenweis, S. M., Collett, J. L., Engling, G., and Malm, W. C.: Aerosol hygroscopicity and cloud droplet activation of extracts of filters from biomass burning experiments, J. Geophys. Res.-Atmos., 113, 9, 10.1029/2007jd009274, 2008.

Carslaw, K. S., Lee, L. A., Reddington, C. L., Pringle, K. J., Rap, A., Forster, P. M., Mann, G. W., Spracklen, D. V., Woodhouse, M. T., Regayre, L. A., and Pierce, J. R.: Large contribution of natural aerosols to uncertainty in indirect forcing, Nature, 503, 67-+, 10.1038/nature12674, 2013.

Chang, D. Y., Lelieveld, J., Tost, H., Steil, B., Pozzer, A., and Yoon, J.: Aerosol physicochemical effects on CCN activation simulated with the chemistry-climate model EMAC, Atmospheric Environment, 162, 127-140, 10.1016/j.atmosenv.2017.03.036, 2017.

Clegg, S. L., Brimblecombe, P., and Wexler, A. S.: Thermodynamic model of the system H+-NH4+-SO42--NO3--H2O at tropospheric temperatures, J. Phys. Chem. A, 102, 2137-2154, 10.1021/jp973042r, 1998.

Collins, D. B., Bertram, T. H., Sultana, C. M., Lee, C., Axson, J. L., and Prather, K. A.: Phytoplankton blooms weakly influence the cloud forming ability of sea spray aerosol, Geophys. Res. Lett., 43, 9975-9983, 10.1002/2016gl069922, 2016.

Crosbie, E., Youn, J. S., Balch, B., Wonaschutz, A., Shingler, T., Wang, Z., Conant, W. C., Betterton, E. A., and Sorooshian, A.: On the competition among aerosol number, size and composition in predicting CCN variability: a multi-annual field study in an urbanized desert, Atmos. Chem. Phys., 15, 6943-6958, 10.5194/acp-15-6943-2015, 2015.

DeCarlo, P. F., Slowik, J. G., Worsnop, D. R., Davidovits, P., and Jimenez, J. L.: Particle morphology and density characterization by combined mobility and aerodynamic diameter measurements. Part 1: Theory, Aerosol Sci. Technol., 38, 1185-1205, 10.1080/027868290903907, 2004.

Hameri, K., O'Dowd, C. D., and Hoell, C.: Evaluating measurements of new particle concentrations, source rates, and spatial scales during coastal nucleation events using condensation particle counters, J. Geophys. Res.-Atmos., 107, 11, 10.1029/2001jd000411, 2002.

Hartz, K. E. H., Tischuk, J. E., Chan, M. N., Chan, C. K., Donahue, N. M., and Pandis, S. N.: Cloud condensation nuclei activation of limited solubility organic aerosol, Atmospheric Environment, 40, 605-617, 10.1016/j.atmosenv.2005.09.076, 2006.

Heim, M., Kasper, G., Reischl, G., and Gerhart, C.: Performance of a New Commercial Electrical Mobility Spectrometer, Aerosol Sci. Technol., 38, 3-14, 10.1080/02786820490519252, 2004.

567 Hermann, M., Wehner, B., Bischof, O., Han, H. S., Krinke, T., Liu, W., Zerrath, A., and Wiedensohler,
568 A.: Particle counting efficiencies of new TSI condensation particle counters, J. Aerosol. Sci., 38, 674-
569 682, 10.1016/j.jaerosci.2007.05.001, 2007.
570 Hudson, J. G.: An Instantaneous CCN Spectrometer, J. Atmos. Ocean. Technol., 6, 1055-1065,
571 10.1175/1520-0426(1989)006<1055:aics>2.0.co;2, 1989.
572 IPCC, 2013: Summary for Policymakers, Intergovernmental Panel on Climate Change, Cambridge
573 University Press, 14, 2013.
574 Jokinen, V., and Makela, J. M.: Closed-loop arrangement with critical orifice for DMA sheath excess
575 flow system, J. Aerosol. Sci., 28, 643-648, 10.1016/s0021-8502(96)00457-0, 1997.
576 Karydis, V. A., Capps, S. L., Russell, A. G., and Nenes, A.: Adjoint sensitivity of global cloud droplet
577 number to aerosol and dynamical parameters, Atmos. Chem. Phys., 12, 9041-9055, 10.5194/acp-12-
578 9041-2012, 2012.
579 Kawecki, S., and Steiner, A. L.: The Influence of Aerosol Hygroscopicity on Precipitation Intensity
580 During a Mesoscale Convective Event, J. Geophys. Res.-Atmos., 123, 424-442, 10.1002/2017jd026535,
581 2018.
582 Knutson, E. O., and Whitby, K. T.: Aerosol classification by electric mobility: apparatus, theory, and
583 applications, J. Aerosol. Sci., 6, 443-451, https://doi.org/10.1016/0021-8502(75)90060-9, 1975.
584 Koehler, K. A., Kreidenweis, S. M., DeMott, P. J., Prenni, A. J., Carrico, C. M., Ervens, B., and
585 Feingold, G.: Water activity and activation diameters from hygroscopicity data - Part II: Application to
586 organic species, Atmos. Chem. Phys., 6, 795-809, 10.5194/acp-6-795-2006, 2006.
587 Kumar, P. P., Broekhuizen, K., and Abbatt, J. P. D.: Organic acids as cloud condensation nuclei:
588 Laboratory studies of highly soluble and insoluble species, Atmos. Chem. Phys., 3, 509-520, 2003.
589 Lance, S., Medina, J., Smith, J. N., and Nenes, A.: Mapping the operation of the DMT Continuous Flow
590 CCN counter, Aerosol Sci. Technol., 40, 242-254, 10.1080/02786820500543290, 2006.
591 Liu, X. H., and Wang, J. A.: How important is organic aerosol hygroscopicity to aerosol indirect
592 forcing?, Environ. Res. Lett., 5, 10, 10.1088/1748-9326/5/4/044010, 2010.
593 Mamakos, A., Ntziachristos, L., and Sarnaras, Z.: Diffusion broadening of DMA transfer functions.
594 Numerical validation of Stolzenburg model, J. Aerosol. Sci., 38, 747-763,
595 10.1016/j.jaerosci.2007.05.004, 2007.
596 Mei, F., Fu, H. J., and Chen, D. R.: A cost-effective differential mobility analyzer (cDMA) for multiple
597 DMA column applications, J. Aerosol. Sci., 42, 462-473, 10.1016/j.jaerosci.2011.04.001, 2011.
598 Moore, R. H., Raatikainen, T., Langridge, J. M., Bahreini, R., Brock, C. A., Holloway, J. S., Lack, D.
599 A., Middlebrook, A. M., Perring, A. E., Schwarz, J. P., Spackman, J. R., and Nenes, A.: CCN Spectra,
600 Hygroscopicity, and Droplet Activation Kinetics of Secondary Organic Aerosol Resulting from the 2010
601 Deepwater Horizon Oil Spill, Environ. Sci. Technol., 46, 3093-3100, 10.1021/es203362w, 2012.
602 Ovadnevaite, J., Ceburnis, D., Martucci, G., Bialek, J., Monahan, C., Rinaldi, M., Facchini, M. C.,
603 Berresheim, H., Worsnop, D. R., and O'Dowd, C.: Primary marine organic aerosol: A dichotomy of low
604 hygroscopicity and high CCN activity, Geophys. Res. Lett., 38, 5, 10.1029/2011gl048869, 2011.
605 Petters, M. D., and Kreidenweis, S. M.: A single parameter representation of hygroscopic growth and
606 cloud condensation nucleus activity, Atmos. Chem. Phys., 7, 1961-1971, 10.5194/acp-7-1961-2007,
607 2007.
608 Petters, M. D., and Kreidenweis, S. M.: A single parameter representation of hygroscopic growth and
609 cloud condensation nucleus activity - Part 3: Including surfactant partitioning, Atmos. Chem. Phys., 13,
610 1081-1091, 10.5194/acp-13-1081-2013, 2013.
611 Rogers, R. R., and Yau, M. K.: in: A Short Course In Cloud Physics, Third ed., edited by: Haar, D. T.,
612 Elsevier Science Inc., Tarrytown, New York, USA, 87-89, 1989.
613 Rose, D., Gunthe, S. S., Mikhailov, E., Frank, G. P., Dusek, U., Andreae, M. O., and Poschl, U.:
614 Calibration and measurement uncertainties of a continuous-flow cloud condensation nuclei counter

615 (DMT-CCNC): CCN activation of ammonium sulfate and sodium chloride aerosol particles in theory
616 and experiment, Atmos. Chem. Phys., 8, 1153-1179, 10.5194/acp-8-1153-2008, 2008.
617 Scanning Mobility Particle Sizer Series 5.400 and 5.500, Grimm Aerosol Technik, Ainring, Germany,
618 2009.
619 Schmale, J., Henning, S., Decesari, S., Henzing, B., Keskinen, H., Sellegri, K., Ovadnevaite, J., Pohlker,
620 M. L., Brito, J., Bougiatioti, A., Kristensson, A., Kalivitis, N., Stavroulas, I., Carbone, S., Jefferson, A.,
621 Park, M., Schlag, P., Iwamoto, Y., Aalto, P., Aijala, M., Bukowiecki, N., Ehn, M., Frank, G., Frohlich,
622 R., Frumau, A., Herrmann, E., Herrmann, H., Holzinger, R., Kos, G., Kulmala, M., Mihalopoulos, N.,
623 Nenes, A., O'Dowd, C., Petaja, T., Picard, D., Pohlker, C., Poschl, U., Poulain, L., Prevot, A. S. H.,
624 Swietlicki, E., Andreae, M. O., Artaxo, P., Wiedensohler, A., Ogren, J., Matsuki, A., Yum, S. S.,
625 Stratmann, F., Baltensperger, U., and Gysel, M.: Long-term cloud condensation nuclei number
626 concentration, particle number size distribution and chemical composition measurements at regionally
627 representative observatories, Atmos. Chem. Phys., 18, 2853-2881, 10.5194/acp-18-2853-2018, 2018.
628 Sem, G. J.: Design and performance characteristics of three continuous-flow condensation particle
629 counters: a summary, Atmos. Res., 62, 267-294, 10.1016/s0169-8095(02)00014-5, 2002.
630 Seol, K. S., Tsutatani, Y., Camata, R. P., Yabumoto, J., Isomura, S., Okada, Y., Okuyama, K., and
631 Takeuchi, K.: A differential mobility analyzer and a Faraday cup electrometer for operation at 200-930
632 Pa pressure, J. Aerosol. Sci., 31, 1389-1395, 10.1016/s0021-8502(00)00037-9, 2000.
633 Sinnarwalla, A. M. a. A., D.J.: A Cloud Nucleus Counter with Long Available Growth Time, Journal of
634 Applied Meteorology, 831-835, 1973.
635 Stratmann, F., Kauffeldt, T., Hummes, D., and Fissan, H.: Differential electrical mobility analysis: A
636 theoretical study, Aerosol Sci. Technol., 26, 368-383, 10.1080/02786829708965437, 1997.
637 Sullivan, R. C., Moore, M. J. K., Petters, M. D., Kreidenweis, S. M., Roberts, G. C., and Prather, K. A.:
638 Timescale for hygroscopic conversion of calcite mineral particles through heterogeneous reaction with
639 nitric acid, Phys. Chem. Chem. Phys., 11, 7826-7837, 10.1039/b904217b, 2009.
640 Svenningsson, B., Rissler, J., Swietlicki, E., Mircea, M., Bilde, M., Facchini, M. C., Decesari, S., Fuzzi,
641 S., Zhou, J., Monster, J., and Rosenorn, T.: Hygroscopic growth and critical supersaturations for mixed
642 aerosol particles of inorganic and organic compounds of atmospheric relevance, Atmos. Chem. Phys., 6,
643 1937-1952, 10.5194/acp-6-1937-2006, 2006.
644

Notation	
$\alpha_{CC}, \beta_{CC}, \gamma_{CC}$	Empirically-determined constants used to calculate Cunningham slip correction factor
Z_p	Aerosol particle electrical mobility
C_C	Cunningham slip correction factor
d_m	Electrical mobility diameter
n	Number of charges on particle
e	Elementary unit of charge
η	Gas dynamic viscosity
λ	Mean free path
Q_{sh}	Sheath flow
Q_e	Excess air flow
Q_a	Aerosol flow
Q_s	Sample flow
κ_{app}	Apparent hygroscopicity parameter
$\kappa_{app,artifact}$	Apparent hygroscopicity parameter artifact
s	Equilibrium water vapor saturation
s_{crit}	Critical saturation (50 % of aerosols active as cloud condensation nuclei)
A	Constant used in calculating κ_{app}
σ_{lv}	Surface tension of water
T	Temperature
D_{act}	Activation diameter
SS_{crit}	Critical percent supersaturation
α_{TF}	Height of DMA transfer function
β_{TF}	Half-width of DMA transfer function
Z_p'	Mobility of particle at DMA inlet
$Z_{p,mid}$	Midpoint of transfer function
ΔZ_p	Half-width of transfer function
V_0	Voltage selected at DMA
r_1	DMA inner radius
r_2	DMA outer radius
L	DMA length
d_{50}	50 %-cut-off diameter

645

646
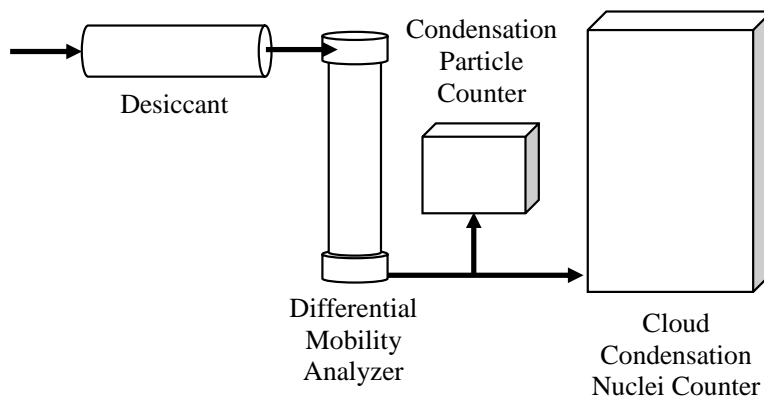
Figure 1 Experimental setup for CCN measurements.
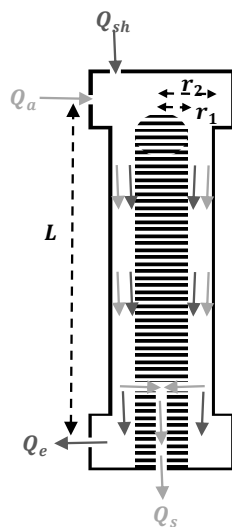
648

649 **Figure 2** Simplified flow diagram of a DMA with an inner electrode radius r_1, outer electrode radius r_2,

650 and distance between aerosol inlet and sample outlet L. Q_{sh} represents the clean sheath air flow, Q_a

651 represent the aerosol flow, Q_e represents the excess air flow, and Q_s represents the sample air flow.
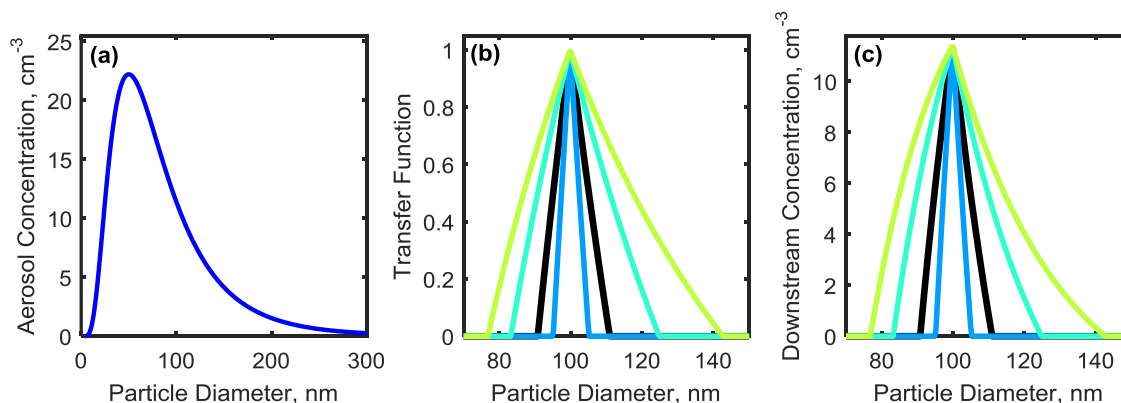
652

653

654 **Figure 3** (a) A theoretical aerosol distribution generated using a lognormal function centered at 50 nm.

655 The total concentration for this distribution is 2000 particles/cm^3. (b) The transfer function calculated

656 using Eq. (7). (c) Downstream aerosol concentration, cm^{-3} (Distribution x transfer function = downstream

657 concentration).

Table 1 Theoretical DMA Flow Test Cases						
Case	Q_{sh} (L min^{-1})	Q_e (L min^{-1})	Q_a (L min^{-1})	Q_s (L min^{-1})	Q_a/Q_{sh}	Q_e/Q_{sh}
DMA 1	3	3	0.3	0.3	0.1	1
DMA 2	3	3	0.15	0.15	0.05	1
DMA 3	3	3	0.6	0.6	0.2	1
DMA 4	3	3	0.9	0.9	0.3	1
DMA 5	3	3.06	0.36	0.3	0.12	1.02
DMA 6	3	3.15	0.45	0.3	0.15	1.05
DMA 7	3	2.94	0.24	0.3	0.08	0.98

658

Table 2 Predicted downstream particle diameter range for each DMA case.

Case	25 nm	50 nm	100 nm	200 nm
DMA 1	23-27	46-56	91-111	181-222
DMA 2	24-26	48-53	95-105	190-211
DMA 3	21-31	42-62	83-125	167-250
DMA 4	20-36	39-71	77-143	154-285
DMA 5	23-27	45-55	90-110	181-220
DMA 6	22-27	45-54	89-107	178-215
DMA 7	23-28	46-56	92-112	183-225

659

660
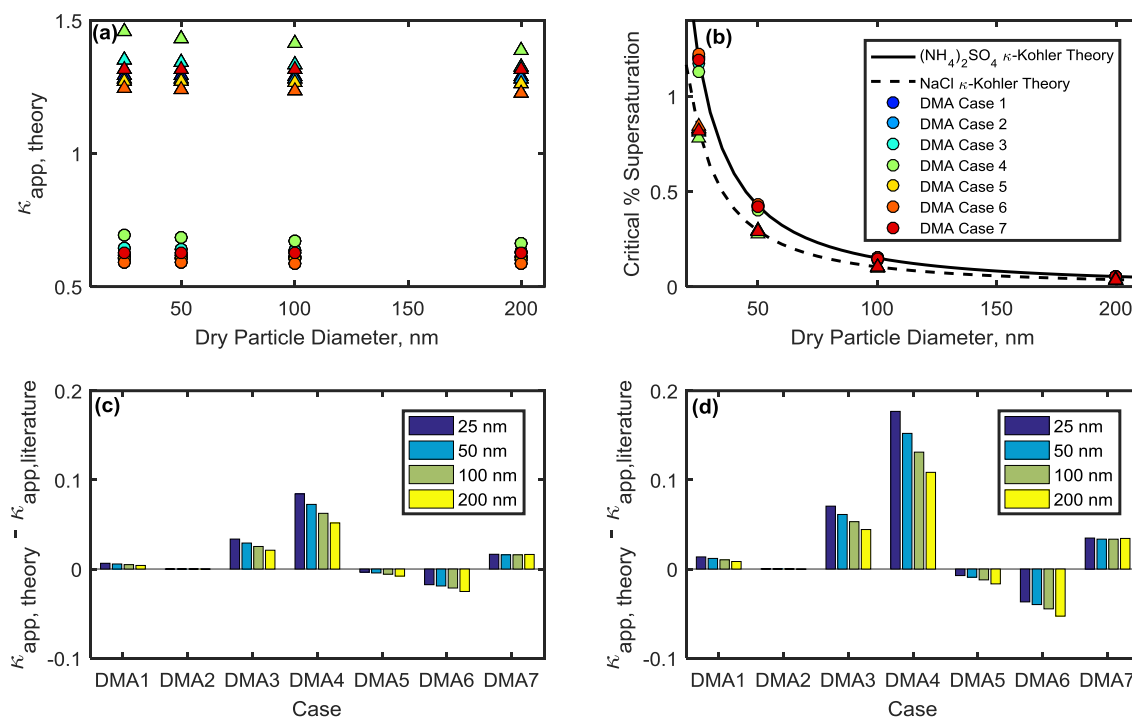
Figure 4 (a) Apparent hygroscopicity κ_{app} for each DMA case. Triangles represent the results for

sodium chloride, and circles represent the results for ammonium sulfate; only one is shown in (b) to

conserve space. (b) The critical supersaturation of ammonium sulfate and sodium chloride particles

calculated for Cases 1-7 using κ_{app} values derived in (a). Ammonium sulfate and sodium chloride

curves from κ-Köhler theory are shown for comparison. (c,d) DMA-flow-derived artifacts in κ_{app} for

ammonium sulfate are shown for each DMA case for ammonium sulfate aerosols and sodium chloride

aerosols.

Table 3 Parameters used in investigating κ_{app} artifacts for low concentrations measured by a condensation particle counter.

Case	d_{50}, nm	Maximum Counting Efficiency
CPC 1	15	100 %
CPC 2	10	100 %
CPC 3	5	100 %
CPC 4	10	90 %
CPC 5	10	95 %
CPC 6	10	98 %

668
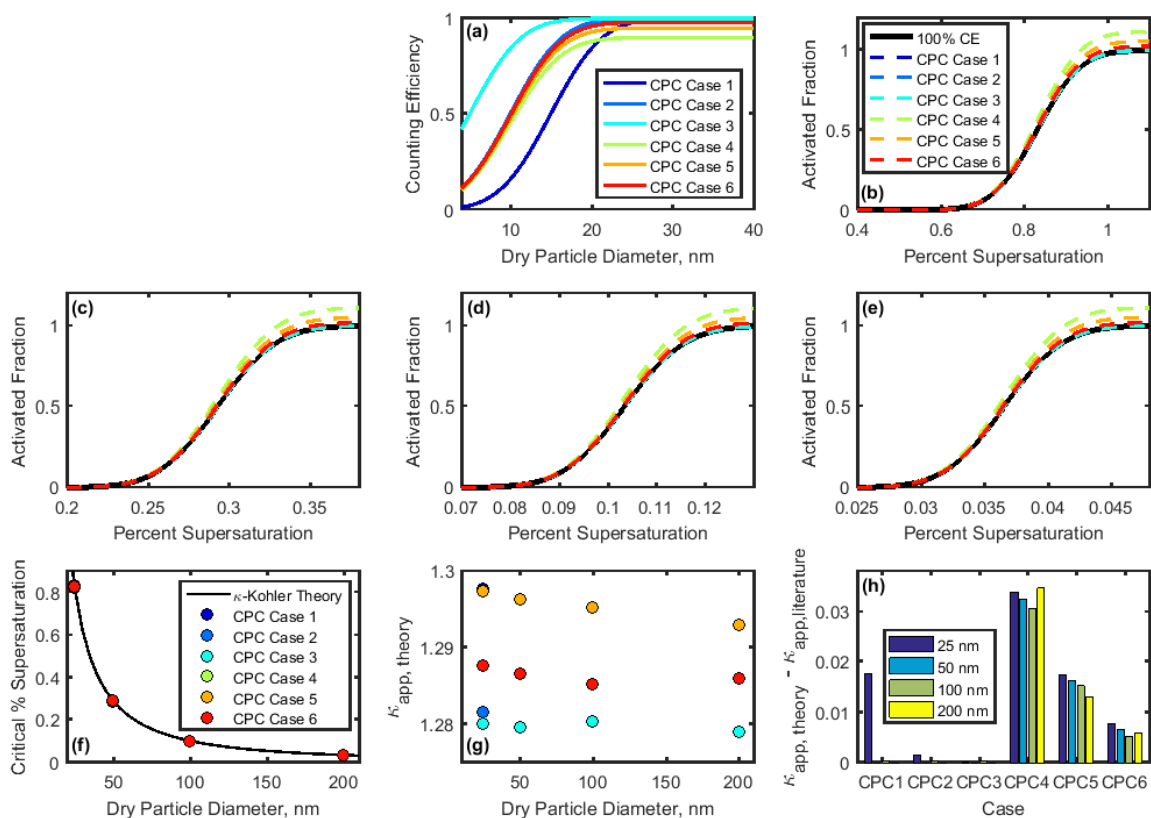
669

670 **Figure 5** (a) Counting efficiency curves based on CPC measurements.

671 (b-e) CCN activation for 25, 50, 100, and 200 nm NaCl, respectively. (f) Critical supersaturation

672 calculated for each activated fraction curve. (g) Apparent hygroscopicity for each case. (h) κ_{app}

673 artifacts for each case.

Table 4 Equations used to model the relationship between a reference or "true" aerosol concentration x (particles cm^{-3}), and the concentration measured by a condensation particle counter y (particles cm^{-3}).

Case	Equation
CPC 7	$y = x - 2 \times 10^{-6} x^2$
CPC 8	$y = 40000 \, \mathrm{erf}\left(\dfrac{x}{32000\sqrt{2}}\right)$
CPC 9	$y = 20000 \, \mathrm{erf}\left(\dfrac{x}{16000\sqrt{2}}\right)$
CPC 10	$y = 10000 \, \mathrm{erf}\left(\dfrac{x}{8000\sqrt{2}}\right)$

674

675
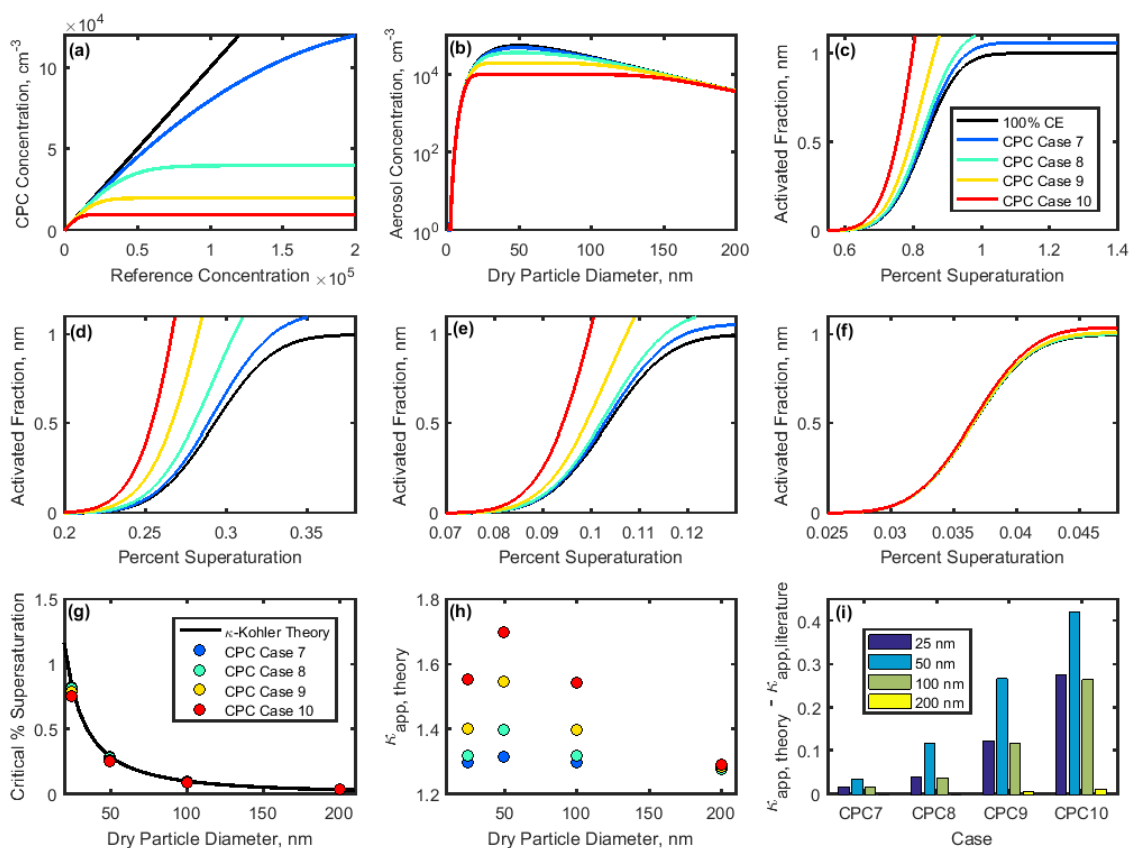
Figure 6 (a) Theoretical relationships between the reference aerosol concentration and CPC

concentration. (b) Concentration-dependent counting efficiencies were applied to a theoretical aerosol

distribution. The ideal case (100 % counting efficiency), shown in black, is a lognormal distribution

centered at 50 nm, consisting of 5×10^6 total particles. (c-f) Activated fraction for 25, 50, 100, and 200

nm NaCl aerosol, respectively. (g,h) Critical supersaturation and apparent hygroscopicity for each

concentration-dependent case. (i) κ_{app} artifacts for each case.

Table 5 Total concentrations used in theoretical aerosol distribution for CCN-derived κ_{app} artifacts.

Case	Total Concentration (particles cm^{-3})
CCN 1	5×10^6
CCN 2	1×10^5
CCN 3	1×10^4
CCN 4	2×10^3

682

683
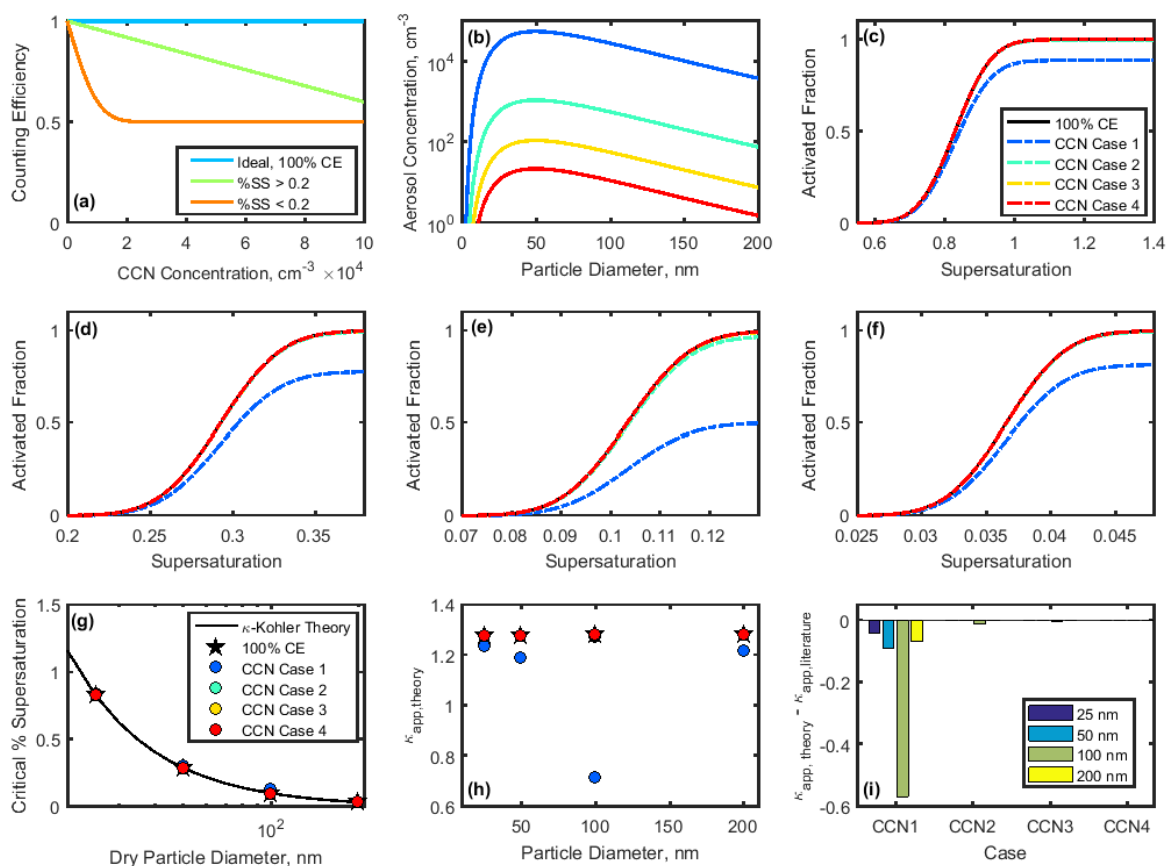
Figure 7 (a) Counting efficiency of the DMT CCN-100. (b) Lognormal distributions used to study CCN

undercounting at high concentrations. (c-f) Activation fractions for 25-200 nm NaCl particles,

respectively. Supersaturation-specific counting efficiencies from (a) were applied to theoretical sigmoid

curves for NaCl CCN activation. Activated fraction in the case of 100 % counting efficiency is shown

for comparison. (g) Critical supersaturation for each case. (h) κ_{app} calculated for each case. (i) κ_{app}

artifacts for each case.

690
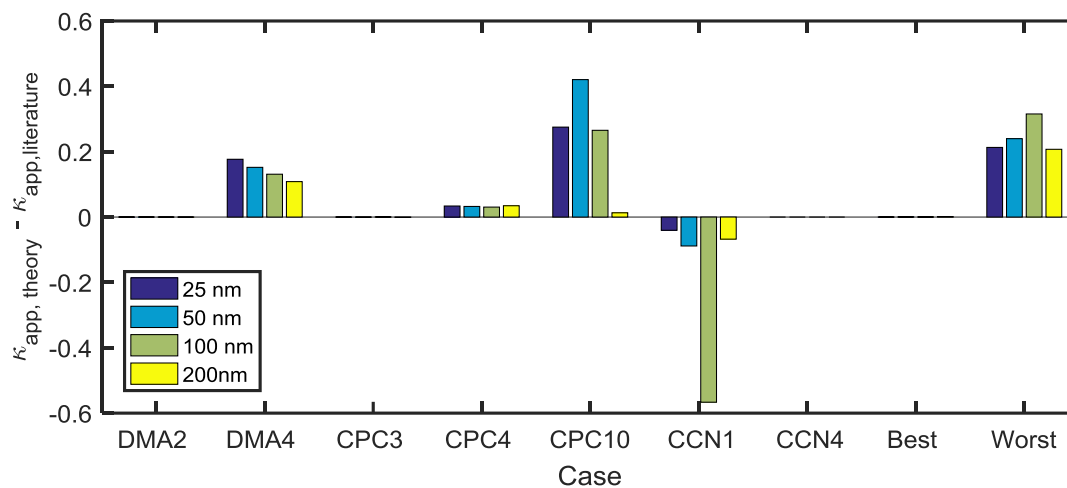
Figure 8 Comparison of κapp artifacts derived from best and worst case scenarios for instrumental

measurements for sodium chloride.   Combined artifacts for the lowest-artifact cases (Best: DMA Case

2, CPC Case 3, and CCN Case 4) and the highest-artifact cases (Worst: DMA Case 4, CPC Case 4, CPC

Case 8, and CCN Case 1).

695